

Supplementary Information

Ultrafast Acoustic Vibrations of Au–Ag Nanoparticles with Varying Elongated Structures

Xin Zhao,^a Zhaogang Nie,^{ab} Yuhua Feng,^c Weiren Zhao,^a Jiahua Zhang,^d Wenchun Zhang,^e*

Paolo Maioli,^{f} Zhi-Heng Loh^b*

*^a School of Physics and Optoelectronic Engineering, Guangdong University of Technology,
Guangzhou 510006, Guangdong, China*

*^b Division of Chemistry and Biological Chemistry, School of Physical and Mathematical
Sciences, Nanyang Technological University, 21 Nanyang Link, Singapore 637371, Singapore*

*^c Institute of Advanced Synthesis, School of Chemistry and Molecular Engineering, Nanjing Tech
University, Nanjing 211816, Jiangsu, China*

*^d State Key Laboratory of Luminescence and Applications, Changchun Institute of Optics, Fine
Mechanics and Physics, Chinese Academy of Sciences, Changchun 130033, China*

*^e College of Traditional Chinese Medicine, Jiangxi University of Traditional Chinese Medicine,
Nanchang 33004, China*

*^f University of Lyon, Université Claude Bernard Lyon 1, CNRS, Institut Lumière Matière, F-
69622, Villeurbanne, France*

*Corresponding authors. E-mail: zgnie@gdut.edu.cn and paolo.maioli@univ-lyon1.fr

1. Sample Synthesis Methods

The samples used in this work were chemically synthesized using a seed-mediated growth technique in aqueous solution, described in detail in ref. S1. In brief, citrate-stabilized Au or Ag nanoparticles (NPs) with 2-mercaptobenzoimidazole-5-carboxylic acid (MBIA) ligands were used as seeds for growing Ag. Controlling the surface energy of the MBIA-modified Au or Ag seeds is the dominant factor for the choice of growth mode of silver, reflecting into the final dimer morphology. Ag atoms generated in the growth solution deposit indeed on the whole surface of the seeds, forming a uniform thin Ag layer. Due to the strong interaction between –SH group and the Au or Ag seed surface, a fraction of MBIA ligands adsorbed on seed surface remain during Ag deposition. As a result, these ligands are embedded under the thin Ag layer as defect sites, causing lattice strain in the Ag layer, this strain increasing with increasing Ag layer thickness. When the strain reaches a critical level, the growth mode of Ag evolves from FM (Frank–van der Merwe or layer-by-layer growth mode) to SK (Stranski–Krastanov growth mode or island-on-layer growth mode).^{S2,S3} By varying ligand conditions (MBIA-concentration and incubation temperature) during the growth of Ag on Au or Ag seeds, the morphology of hybrid nanoparticles can thus be continuously tuned from concentric to eccentric core-shell, acorn-like shapes and dimers. The growth of Ag island in the case of Ag–Ag dimers (sample 1) and Au@Ag–Ag acorn-shaped dimers (sample 2) follows a SK growth mode. Sample 3, containing eccentric core–shell spheroids, can be viewed as intermediate between FM and SK modes.

More specifically, for the samples with Au seeds, 1 mL of as-synthesized AuNPs ($d = 50$ nm, 157 pM in number of NPs) were incubated with MBIA. After 2-hour incubation at room temperature, reductant hydroquinone (HQ, 0.5 mM) was added to this solution, followed by

dropwise addition of AgNO_3 (0.5 mM) to initiate the reaction. Au@Ag–Ag acorn-shaped dimers (sample 2) were prepared by incubating pure AuNPs with 20 μM MBIA at 60 °C, while for the Au@Ag eccentric core-shell spheroids (sample 3), AuNPs were incubated with 5 μM MBIA at room temperature, to obtain a lower MBIA concentration.

The growth of Ag on MBIA-modified AgNPs (sample 1) is very similar, by only changing the metal seeds.^{S1} As mentioned in main text, the NPs seeds used for synthesis of Ag–Ag dimers (sample 1) in fact were not monometallic Ag spheres but Au@Ag core-shell nanoparticles of ~65 nm in diameter made of an inner ~10–15 nm diameter Au core embedded in a Ag shell, synthesized following literature reports.^{S1,S4} Using the small Au core was necessary to synthesize AgNPs of this size with low size dispersion. The dimers were then obtained by incubating 20 μL MBIA ligands with 1 mL seeds at 60 °C for 2 h before Ag deposition. Nevertheless, as the fraction of Au atoms is very small (<1%) and its influence on low-frequency vibrational modes negligible, as discussed in the main text, for simplicity they are referred to as Ag–Ag dimers.

2. Pump-probe Experiment

Optical pump-probe spectroscopy was performed using very broadband pump pulses with ~500 to 900 nm spectral range and narrowband probe pulses in the ~540–590 nm range (Fig. S1a–b and Fig. 1d). The broadband laser pulses are produced by spectral broadening the output from an amplified Ti:sapphire laser system (4.6 mJ, 25 fs, 1 kHz) in a helium-filled hollow-core-fiber followed by chirped mirror compression. The detailed pulse generation method was reported in our previous work.^{S5} The narrowband probe pulse centered at 550 nm is generated by inserting a band-pass filter into the original broadband laser pulse. Typical pulse energies for

pump and probe beams are 200 and 20 nJ, respectively. The focal spot diameter ($1/e^2$) of the pump beam ($400\ \mu\text{m}$) is twice that of the probe beam ($200\ \mu\text{m}$).

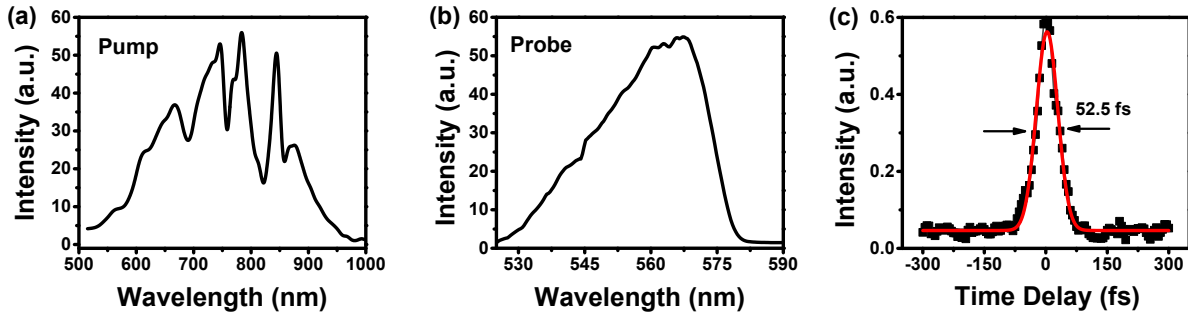


Fig. S1 Optical spectra of (a) pump and (b) probe pulses, and (c) intensity cross-correlation trace of pump and probe pulses, revealing a time resolution of 52.5 fs fwhm for the apparatus.

The transmitted probe beam is spectrally dispersed in a 300 mm spectrograph and detected by a 1024-element linear array detector, with a read-out rate of 1 kHz and synchronized to a 500 Hz optical chopper positioned in the path of pump beam (as for time-resolved signals in Fig. S2). For increasing the signal-to-noise ratio (as in the case of signals shown in Fig. 2 in main text), synchronous detection with longer integration times is made using a photodiode and lock-in amplifier replacing the spectrograph and array detector. A band-pass filter centered at 570 nm with a 10 nm bandwidth is positioned before the photodiode for narrowband signal filtering. The time resolution of the experimental apparatus is measured by performing a second-order pump-probe intensity cross-correlation with a 10- μm -thick BBO crystal located at the sample position. The resultant cross-correlation trace yields a time resolution of 52.5 fs fwhm for the apparatus (Fig. S1c).

3. Time-resolved differential transmission signals

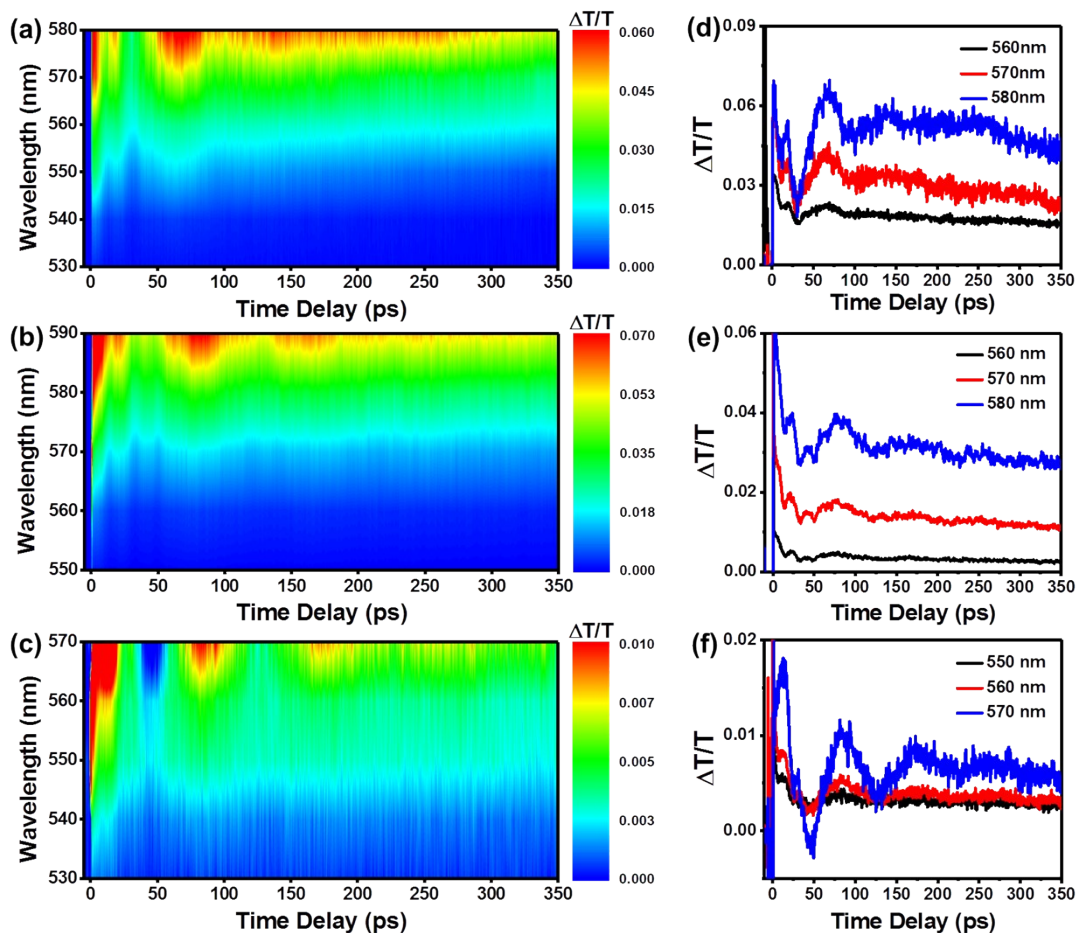


Fig. S2 Two-dimensional color maps of $\Delta T/T$ spectra of (a) Ag-Ag dimers, (b) Au@Ag-Ag acorn-shaped heterodimers, and (c) Au@Ag core-shell eccentric spheroids. Color scale, vertical and horizontal axes correspond to $\Delta T/T$ amplitude, probe wavelength and pump-probe time delay, respectively. (d-f) Corresponding transient absorption signals at selected probe wavelengths, vertically offset for clarity.

4. FEM

FEM (Finite Element Modeling) is used to numerically compute the vibrational modes of metal nano-objects, which in most cases present arbitrary and complex displacement profiles. As the synthesized nanocrystals are polycrystalline,^{S1} Au and Ag polycrystalline elastic constants were introduced in FEM computations ($E_{\text{Au}} = 79.4$ GPa, $\nu_{\text{Au}} = 0.424$, $\rho_{\text{Au}} = 19284$ Kg/m³; $E_{\text{Ag}} = 82.45$ GPa, $\nu_{\text{Ag}} = 0.364$, $\rho_{\text{Ag}} = 10501$ Kg/m³, where E is the Young's modulus, ν is Poisson ratio and ρ is the density).^{S6} Note that different sets of elastic constants are reported and may lead to slightly different computed periods.^{S6,S7}

A delicate point in the FEM analysis is to recognize the modes which can be excited and detected efficiently by pump-probe spectroscopy.^{S8} As vibrations are launched by thermal dilation of the particles, the most excited modes are those whose corresponding displacement profile best matches particle dilation. To select these modes, the integral over the entire nano-object volume of the scalar product between the radial displacement induced by particle dilation and the one corresponding to the mode is thus systematically computed, all modes leading to a null scalar product being ruled out. A visual analysis of the displacement profile allows to further identify vibrational modes relevant for the analysis.

5. TEM, Absorption spectra, time-resolved signals and vibrational analysis of Au nanorods

Seed-mediated chemical synthesis is also used to produce monocrystalline Au nanorods in aqueous surfactant solutions, following the approach described in ref. S9. Their TEM images (leading to nanorods length of 109 ± 10 nm and diameter of 55 ± 6 nm) and steady-state

absorption spectrum are shown in Fig. S3a–b. Time-resolved transient absorption signal with a 570 nm probe wavelength and its fit by Equation (1) of main text are presented in Fig. S3c, together with the Fourier Transform of $\Delta T/T$ oscillating contributions (Fig. S3d). In analogy with the case of all elongated nano-objects discussed in the main text, both fit in the time-domain and Fourier Transform of nanorods $\Delta T/T$ signals indicate two distinct vibrational modes, with periods (21 ± 1) ps and (116 ± 9) ps, which are identified via FEM modeling as nanorod radial breathing (RBM) and axial stretching (ASM) vibrational modes, their computed displacement profiles being shown in Fig. S3e–f. Nanorods are modeled as cylinders with 55 nm diameter and 54 nm length capped with two hemispheres with radius 27.5 nm.

Crystallinity of the synthesized nanorods (long axis parallel to [110] crystal direction)^{S9} has been considered in FEM computations, by introducing elastic constants $c_{11} = 192$ GPa, $c_{12} = 163$ GPa, and $c_{44} = 42$ GPa.^{S11} Displacement profiles are visually affected by lattice crystallinity, with anisotropic structures particularly visible in the ASM profile (Fig. S3f).

Agreement between experimentally-detected vibrational periods and FEM-computed ones is good (see Table S1). Computed RBM period matches the one experimentally measured. The ~10% discrepancy between experimental and numerical ASM periods ((116 ± 9) ps and 102.5 ps respectively) probably comes from the $\pm 10\%$ dispersion in nanorods length, optical time-resolved signals being dominated by larger particles with longer vibrational periods.^{S12,S13} Crystallinity has a strong impact on the predicted ASM period, which is expected to be 30% larger for nanorods with long axis in the [100] directions (Table S1), while FEM-computations with polycrystalline Au elastic constants (the ones used in the main text) would lead to a much shorter ASM period (Table S1). A better experimental-theoretical agreement for the ASM periods would be obtained by using analytical formulas applying to infinitely long cylinders and

is probably fortuitous, approximation to long cylinders being reasonable only for length-over-diameter ratios larger than 2.5.^{S14,S15}

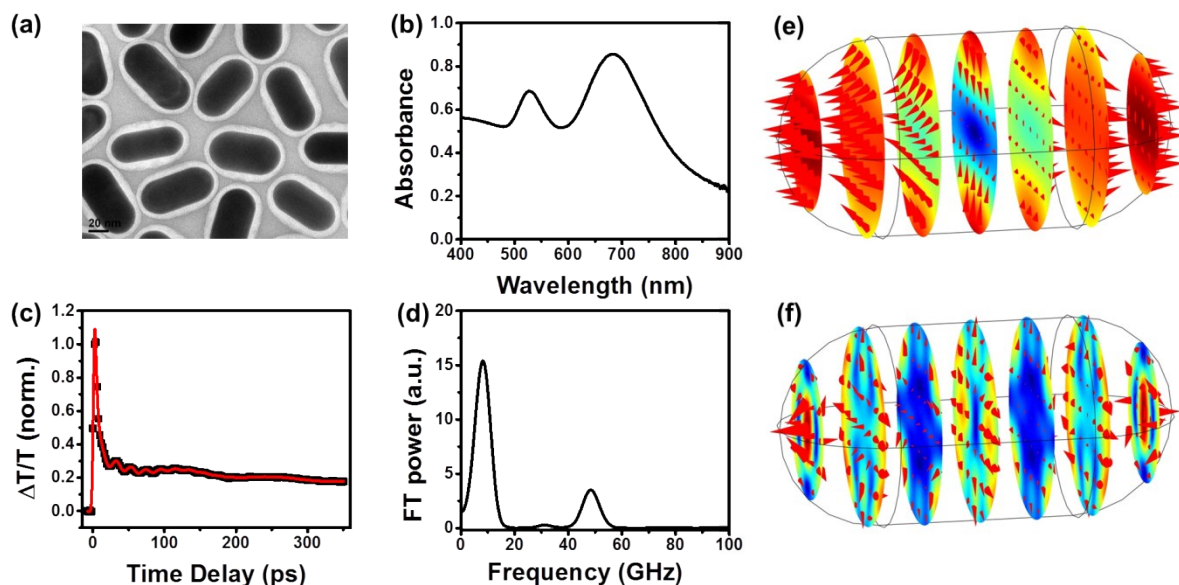


Fig. S3(a) TEM images and (b) absorption spectra of Au nanorods with a length of 109 ± 10 nm and a diameter of 55 ± 6 nm. (c) Normalized $\Delta T/T$ time-resolved signal probed at 570 nm. (d) Fourier Transform of the time-resolved signal after subtraction of exponential decays. FEM-computed displacement profiles of the two most visible pump-induced vibrational modes, (e) ASM and (f) RBM. Arrows and color represent the directions and the amplitudes (from blue to red) of displacement vectors.

Vibrational mode	Experiment	FEM [110]	FEM [100]	FEM pc	Cylinder pc
RBM	21 ± 1	21.3	21.6	21.6	22.9
ASM	116 ± 9	102.5	131	95.7	107.4

Table S1. Experimentally-detected and computed RBM and ASM vibrational periods for Au-nanorods with a length of 109 nm and a rod diameter of 55 nm. All values are expressed in picoseconds. FEM computations are made using both single crystal elastic constants (long axis parallel to the lattice orientation indicated) and polycrystalline (pc) gold. The values predicted for an infinitely long cylinder using polycrystalline elastic constants are reported in the last column.

6. FEM-computed displacement profiles of a metal nanosphere and nanospheroid

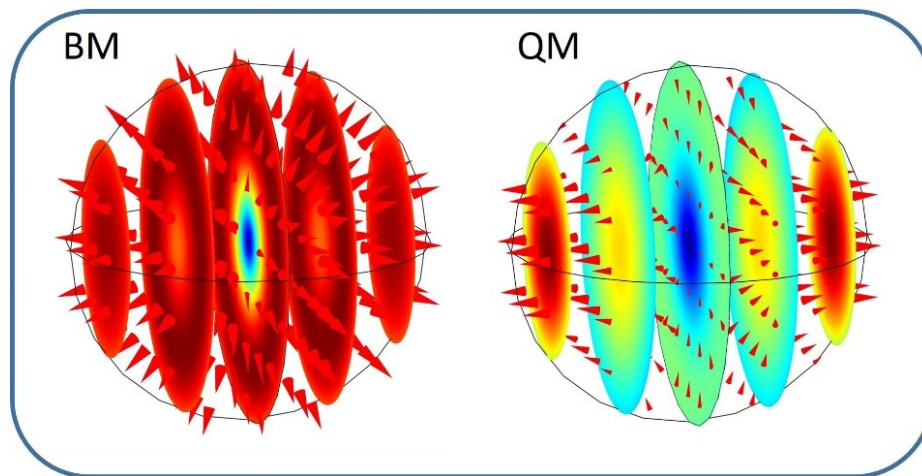


Fig. S4 FEM-computed displacement profiles of the radial breathing mode (left) and quadrupolar mode (right) of a polycrystalline Ag nanosphere with a diameter of 65 nm. Computed periods are 19.8 and 45.4 ps, respectively.

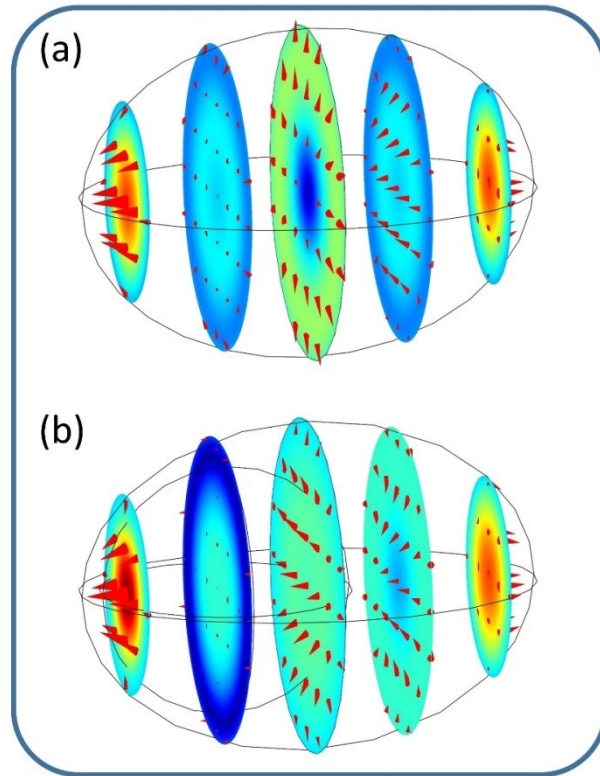


Fig. S5 FEM-computed displacement profiles of first harmonic ASM-like mode for (a) an homogeneous Ag prolate spheroid and (b) eccentric Au@Ag core-shell spheroid, both with a 110 nm long axis and 80 nm minor axes. Computed frequencies are 28.1 and 24.5 GHz, respectively.

References

- (S1) Y. Feng, J. He, H. Wang, Y. Y. Tay, H. Sun, L. Zhu, and H. Chen, *J. Am. Chem. Soc.* 2012, **134**, 2004–2007.
- (S2) M. A. Herman, W. Richter, and H. Sitter, *Epitaxy: Physical Principles and Technical Implementation*, Springer: New York, 2004.
- (S3) Z. Peng, and H. Yang, *Nano Today*, 2009, **4**, 143–164.
- (S4) W. Xie, L. Su, P. Donack, A. Shen, X. Zhou, M. Sackmann, A. Materny and J. Hu, *Chem. Commun.*, 2009, **35**, 5263–5265.
- (S5) Z. Nie, R. Long, J. Li, Y. Y. Zheng, O. V. Prezhdo, and Z.-H. Loh, *J. Phys. Chem. Lett.*, 2013, **4**, 4260–4266.
- (S6) H. Ledbetter and S. Kim, *Monocrystal Elastic Constants and Derived Properties of the Cubic and the Hexagonal Elements: in Handbook of Elastic Properties of Solids, Liquids, and Gases*, Academic Press: New York, 2001
- (S7) H. E. Saucedo, D. Mongin, P. Maioli, A. Crut, M. Pellarin, N. D. Fatti, F. Vallée, and I. L. Garzón, *J. Phys. Chem. C* 2012, **116**, 25147–25156
- (S8) A. Crut, P. Maioli, N. Del Fatti and F. Vallée, *Phys. Rep.*, 2015, **549**, 1–43.
- (S9) C. J. Orendorff, and C. J. Murphy, *J. Phys. Chem. B.*, 2006, **110**, 3990–3994.
- (S10) A. Gole and C. J. Murphy, *Langmuir*, 2008, **24**, 266–272.
- (S11) J. R. Neighbours, and G. A. Alers, *Phys. Rev.* 1958, **111**, 707–712.
- (S12) G. V. Hartland, *Chem. Rev.*, 2011, **111**, 3858–3887.
- (S13) H. Petrova, J. Perez-Juste, Z. Zhang, J. Zhang, T. Koselc and G. V. Hartland, *J. Mater. Chem.*, 2006, **16**, 3957–3963.

(S14) M. Hu, X. Wang, G. V. Hartland, P. Mulvaney, J. P. Juste, and J. E. Sader, *J. Amer. Chem. Soc.*, 2003, **125**, 14925–14933.

(S15) P. Zijlstra, A. L. Tchebotareva, J. W. M. Chon, M. Gu, and M. Orrit, *Nano Lett.*, 2008, **8**, 3493–3497.